Restoration of Multilayered Single-Photon 3D LiDAR Images

RESTORATION OF MULTILAYERED SINGLE-PHOTON 3D LIDAR IMAGES

Abderrahim Halimi[(1)]*, Ximing Ren*[(1)]*, Aongus McCarthy*[(1)]*,*
Jose Bioucas-Dias[(2)], Stephen McLaughlin[(1)], Gerald S. Buller[(1)]

[(1)] School of Engineering and Physical Sciences, Heriot-Watt University, Edinburgh U.K.
[(2)] Instituto de Telecomunicações and Instituto Superior Técnico, Universidade de Lisboa, Portugal

ABSTRACT

This paper proposes a new algorithm to restore 3D single-photon Lidar images obtained under challenging realistic scenarios which include imaging multilayered targets such as semi-transparent surfaces or imaging through obscurants such as scattering media (e.g., water, fog). The Data restoration and exploitation is achieved by minimising an appropriate cost-function accounting for the data Poisson statistics and the available prior knowledge regarding the depth and reflectivity estimates. The proposed algorithm takes into account (i) the non-local spatial correlations between pixels, by using a convex non-local total variation (TV) regularizer, and (ii) the clustered nature of the returned photons, by using a collaborative sparse prior. The resulting minimization problem is solved using the alternating direction method of multipliers (ADMM) that offers good convergence properties. The algorithm is validated using both synthetic and real data which show the benefit of the proposed strategy in the sparse regime due to a fast acquisition or in presence of a high background due to obscurants.

***Index Terms*—** Lidar waveform, Poisson statistics, image restoration, ADMM, NR3D, collaborative sparsity.

1. INTRODUCTION

3D laser detection and ranging (Lidar) imaging provides rich information regarding the depth profile and reflectivity of observed targets. This is achieved by emitting laser pulses and recording the arrival times of the reflected photons using a time-correlated single-photon counting (TCSPC) module. A histogram of photon counts with respect to (w.r.t.) time-of-flight is then constructed for each pixel. For single-layered surface compact objects, the histogram contains one peak whose location and amplitude are related to the depth and reflectivity of the observed target. In this paper, we are interested in challenging scenarios including: the sparse photon regime that is encountered when reducing the acquisition times or for long-range imaging [1]; the presence of multi-peaks (due to imaging through semi-transparent surfaces or when the laser beam covers many depth surfaces) [2, 3]; and a high background level (e.g. imaging through obscurants) [4].

Although TCSPC-based ranging has a limited shot-noise sensitivity and a fine surface-to-surface resolution, it often requires a restoration step when acquired under real-world scenarios [2, 5, 6]. Many solutions have been proposed in the literature; e.g., [5] considered a Markov chain Monte-Carlo (MCMC) algorithm which showed promising results but a high computational cost; [2, 6] expressed the problem using a convex formulation combining the data statistics and regularization terms leading to faster results. However, the approach in [2] assumes the sparsity of the received photons and may lead to the detection of background noise as a target. The regularization in [6] showed good results for scenes presenting objects well separated in depth, however, it might be inappropriate for targets with distributed depths which will occupy the full depth histogram when considering all the pixels. Further simplifications were adopted in [7], such as the presence of one surface and a Gaussian system impulse response, leading to faster results. However, these assumptions may reduce the impact of this algorithm in real scenarios.

In this paper, we propose a solution to restore 3D images by minimizing a convex function combining the Poisson data statistics, which is expressed using a linear formulation as in [2, 6], with two regularization terms. Because of the data fine resolution and cube sparsity (i.e., sparsity in the 3D domain), both regularizers operate on a low-pass filtered cube, which shows better recovering properties. The first convex term generalizes [6] by accounting for non-local spatial correlations between the reflectivities. The second term assumes the presence of a few number of peaks in each group of local pixels, which is achieved using a local collaborative sparse prior (group-sparsity) [8–10]. The parameters of the resulting formulation are then estimated using an alternating direction method of multipliers (ADMM) algorithm [7, 11–13]. The proposed approach is validated on synthetic and real data showing good results under different conditions.

The paper is organized as follows. The observation model is introduced in Section 2 followed by the description of the proposed approach and estimation algorithm in Section 3. Results on synthetic and real data are presented in Section 4. Conclusions and future work are finally reported in Section 5.

This work was supported by the UK Defence Science and Technology Laboratory (DSTL) and EPSRC Grants EP/J015180/1, EP/N003446/1, EP/M01326X/1, EP/K015338/1, and by the Portuguese Science and Technology Foundation under the Project UID/EEA/50008/2013.

2. OBSERVATION MODEL

The Lidar system operates by sending light pulses and detecting the returned photons and their time of flight from the target. This operation can be repeated for each pixel location when using a scanning system (e.g., raster scan systems [14]) or by directly acquiring an array of pixels (e.g., array based systems [15]). For both approaches, a histogram can be constructed for each pixel by representing the number of received counts with respect to their times-of-arrival. More precisely, the Lidar observation can be gathered in the matrix $\boldsymbol{y}_{n,t}$, where $n \in \{1, \cdots, N\}$ and $t \in \{1, \cdots, K\}$, which represents the number of photon counts within the tth bin of the nth pixel, where N, K are the number of pixels and time bins, respectively. If the laser beam is reflected by a single surface, the histogram will contain a single peak whose amplitude and position are related to the target's reflectivity and depth, respectively. However, when the observed scene contains semi-transparent surfaces, obscurants or the laser beam covers many depth surfaces, the returned signal may contain multiple peaks, located at distances related to the observed depths. This paper principally deals with the multi-peaks and a high level of noise cases due to imaging through obscurants and semi-transparent surfaces. Assuming the observed photon counts $\boldsymbol{y}_{n,t}$ are distributed according to a Poisson distribution $\mathcal{P}(.)$ as follows [16, 17]

$$y_{n,t} \sim \mathcal{P}(s_{n,t}) \tag{1}$$

where

$$s_{n,t} = \sum_{m=1}^{M_n} [r_{n,m} g(t - k_{n,m} T)] + b_n \tag{2}$$

and M_n is the number of layers in the nth pixel, T is the time resolution of the system, $k_{n,m} \geq 0$ is the range's position of the mth object from the sensor (related to its depth), $r_{n,m} \geq 0$ is the mth reflectivity of the target, $b_n \geq 0$ denotes the background and dark counts of the detector, and $g(.)$ represents the system impulse response (SIR) assumed to be known from the calibration step. The discrete time version of (2), when considering K time bins, can be expressed as a linear system (convolution by the SIR) as follows [2]

$$\boldsymbol{s}_n = \boldsymbol{G}\boldsymbol{x}_n \tag{3}$$

where $\boldsymbol{G} = [\boldsymbol{g}_1, \cdots, \boldsymbol{g}_K, \boldsymbol{1}_{K\times 1}]$ is a $K \times (K+1)$ matrix gathering shifted impulse responses, $\boldsymbol{1}_{i\times j}$ denotes the $(i \times j)$ matrix of 1, $\boldsymbol{g}_i = [g(T-iT), g(2T-iT), \cdots, g(KT-iT)]^\top$ is a $(K \times 1)$ vector representing the discrete impulse response centered at iT and $\boldsymbol{x}_n$ is a $(K+1) \times 1$ vector whose value are zero except for $\boldsymbol{x}_n(k_{n,m}) = r_{n,m}, \forall m$, and $\boldsymbol{x}_n(K+1) = b_n$. Using (3), straightforward computations show that the negative-log-likelihood associated with the discrete observations $\boldsymbol{y}_{n,k} \sim \mathcal{P}[(\boldsymbol{G}\boldsymbol{x}_n)_k]$ is given by

$$\mathcal{L}_n(\boldsymbol{x}_n) = \mathcal{H}_n(\boldsymbol{G}\boldsymbol{x}_n) \tag{4}$$

where $\mathcal{H}_n : \mathbb{R}^K \to \mathbb{R} \cup \{-\infty, +\infty\}$ is given by

$$\mathcal{H}_n(\boldsymbol{z}) = \sum_{k=1}^{K} \left\{ z_k - y_{n,k} \log\left[z_k^{(+)}\right] + i_{\mathbb{R}_+}(z_k) \right\} \tag{5}$$

where $z_k^{(+)} = \max\{0, z_k\}$ and $i_{\mathbb{R}_+}(x)$ is the indicator function that imposes non-negativity ($i_{\mathbb{R}_+}(x) = 0$ if x belongs to the non-negative orthant and $+\infty$ otherwise). Finally, assuming independence among the observed pixels conditional on $\boldsymbol{X}$ leads to the following negative-log of the joint likelihood

$$\mathcal{L}(\boldsymbol{X}) = -\log[P(\boldsymbol{Y}|\boldsymbol{X})] = \sum_n \mathcal{L}_n(\boldsymbol{x}_n) \tag{6}$$

where $\boldsymbol{Y}$ (resp. $\boldsymbol{X}$) is a $K \times N$ (resp. $(K+1) \times N$) matrix gathering the vectors $\boldsymbol{y}_n$ (resp. $\boldsymbol{x}_n$). The goal is then to estimate the sparse matrix $\boldsymbol{X}$, where the positions and values of the non-zero elements correspond to the target depths and intensities, respectively.

3. REGULARIZED PROBLEM

Estimating the matrix $\boldsymbol{X}$ is an ill-posed inverse problem that requires the introduction of prior knowledge (or regularization terms) related to the target depths and reflectivities in addition to the data fidelity term $\mathcal{L}(\boldsymbol{X})$ in (6), as follows

$$\mathcal{C}(\boldsymbol{X}) = \mathcal{L}(\boldsymbol{X}) + i_{\mathbb{R}_+}(\boldsymbol{X}) + \tau_1 \phi_1(\boldsymbol{X}) + \tau_2 \phi_2(\boldsymbol{X}) \tag{7}$$

where $\tau_1 > 0$, $\tau_2 > 0$ are two regularization parameters, $i_{\mathbb{R}_+}(\boldsymbol{X}) = \sum_{n,k} i_{\mathbb{R}_+}(x_{n,k})$ and ϕ_1, ϕ_2 are two regularization functions associated with depth and reflectivity, as detailed in the next sub-sections.

3.1. Priors on the support: depth regularization

The detected photons associated with a target are generally clustered inside the cube in contrast to the background counts that spread over the full cube. This paper accounts for this effect by combining the priors used in [2, 6, 18] and provides a solution to their limitations. To separate the noise from the signal return, we assume sparsity of the latter on a downsampled image. This will detect cluster of returns that are probably due to the target, while it will eliminate the isolated counts due to noise. An $\ell_{2,1}$ mixed norm is used to impose collaborative sparsity [8, 10], i.e., sparsity on small cubes obtained by grouping local pixels and depth bins, as follows

$$\phi_1(\boldsymbol{X}) = ||\text{diag}(\boldsymbol{v})\boldsymbol{K}\boldsymbol{F}\boldsymbol{X}(:)||_{2,1} \tag{8}$$

where $\boldsymbol{X}(:) \in \mathbb{R}^{(K+1)N\times 1}$ denotes the vectorization of the matrix $\boldsymbol{X}$, $\boldsymbol{F} \in \mathbb{R}^{KN\times(K+1)N}$ is a matrix that selects the first K rows of $\boldsymbol{X}$ and discard the background row, $\boldsymbol{K} : \mathbb{R}^{KN\times 1} \to \mathbb{R}^{S_b \times N_B}$ is a linear operator that provides an $S_b \times N_B$ matrix as an output where its column gathers the S_b elements of a bloc of size $S_b = (r_b \times c_b \times t_b)$ and N_B denotes the number of these blocs in the data cube and $\boldsymbol{v} \in \mathbb{R}^{N_B \times 1}$ contains weights for each bloc. One can also express

$\phi_1(\boldsymbol{X})$ as follows $\phi_1(\boldsymbol{X}) = \sum_{i=1}^{N_B} v_i \sqrt{\left(\sum_{(t,n)\in\nu_i} x_{n,t}^2\right)}$, where ν_i contains the pixel and time bin indices of the ith bloc.

3.2. Priors on the counts: regularized intensity

To restore the observed count values, the proposed regularization term will exploit the non-local spatial correlation between count values of the image. Non-local approaches have shown promising results to restore natural images (especially textured images) and represent a key ingredient in most state-of-the-art algorithms [19–21]. In this paper, we consider photon-starved regime in which the histograms are sparse and prevent the direct application of spatial correlation regularizations. To solve this problem, the spatial regularization is performed on a low-pass filtered image in the range dimension which improves the separation between the target features and the background noise as highlighted in [6, 22]. To achieve this, each pixel is connected to the other similar pixels in the image (through the consideration of similarity weights $\boldsymbol{W}$) and will benefit from their information to improve its estimate. Under these considerations, the proposed regularization term can be mathematically expressed as

$$\phi_2(\boldsymbol{X}) = ||\boldsymbol{H}_w \boldsymbol{D}_h \boldsymbol{F}\boldsymbol{X}(:)||_F^2 \tag{9}$$

where $\boldsymbol{D}_h \in \mathbb{R}^{K_h N \times KN}$ is a matrix summing the photon counts of each $\#h$ successive time bins, K_h is the integer part of the division K/h, and $\boldsymbol{H}_w \in \mathbb{R}^{n_d K_h N \times K_h N}$ is a block-circulant-circulant-block matrix which computes weighted differences between each pixel and other n_d pixels located in a fixed field (e.g., a large bloc of neighbourhood pixels). More precisely, the operator $\boldsymbol{H}_w : \mathbb{R}^{K_h N} \to \mathbb{R}^{n_d K_h N}$ performs the following operation

$$||\boldsymbol{H}_w \boldsymbol{z}||_F^2 = \sum_{n=1}^{N}\sum_{i=1}^{n_d}\sum_{\ell=1}^{K_h} w_{i,n}^2 \left(H_i^{\text{Diff}} \boldsymbol{z}_\ell\right)^2\Big|_n \tag{10}$$

where $\boldsymbol{z}_\ell \in \mathbb{R}^{N\times 1}$ denotes the ℓth column of a matrix $\boldsymbol{Z} \in \mathbb{R}^{N\times K_h}$ built from $\boldsymbol{z} \in \mathbb{R}^{K_h N\times 1}$ as follows $\boldsymbol{Z} = [\boldsymbol{z}_1, ..., \boldsymbol{z}_{K_h}]$, $H_i^{\text{Diff}} \in \mathbb{R}^{N\times N}$ computes the difference between each pixel and that located at the ith direction (we consider n_d predefined directions or shifts), $w_{i,n}^2$ are the weights associated with the nth pixel and ith direction, and $\boldsymbol{x}|_n$ selects the nth element of $\boldsymbol{x}$. For simplicity, we treat the matrices H_i^{Diff} with periodic boundary conditions as cyclic convolutions. This non-local total variation can also be expressed in matrix form as follows

$$||\boldsymbol{H}_w \boldsymbol{z}||_F^2 = \left|\left| \begin{array}{c} \left\{\mathbb{I}_{K_h} \otimes \left[\text{diag}(\boldsymbol{w}_{1:}) H_1^{\text{Diff}}\right]\right\} \boldsymbol{z} \\ \vdots \\ \left\{\mathbb{I}_{K_h} \otimes \left[\text{diag}(\boldsymbol{w}_{n_d:}) H_{n_d}^{\text{Diff}}\right]\right\} \boldsymbol{z} \end{array} \right|\right|_F^2 \tag{11}$$

where $\otimes$ denotes the Kronecker product and $\mathbb{I}_{K_h}$ is the identity matrix, $\boldsymbol{w}_{i:} \in \mathbb{R}^N$ are the weights associated with the ith direction, and diag is the diagonalization operator.

3.3. Choice of the weights

Setting the weights $\boldsymbol{w}, \boldsymbol{v}$ should reflect our prior knowledge about possible spatial correlations and target's depths. Such information can be extracted from complimentary imaging modalities of the same scene leading to a fusion task. For simplicity, this paper only use the Lidar data to fix these weights. For this, a low-pass spatial filter is applied to the data cube to fill missing pixels and reduce the noise. The classical cross-correlation is then applied iteratively in the resulting data to extract the main k_p peaks of each pixels leading to k_p depth and intensity images. The sum of these intensity images (denoted I) is used to fix the weights $\boldsymbol{w}$ as follows (see also [23])

$$w_{ij} = \max\left[0.5, \exp\left(-\frac{|I_i - I_j|}{\sigma_w}\right)\right]. \tag{12}$$

To fix $\boldsymbol{v}$, we build a data cube $\tilde{\boldsymbol{y}}$ by associating to each cross-correlation depth location the corresponding intensity value. The resulting cube is then downsampled to form N_B groups of size S_b. The groups with higher intensities are assigned lower coefficient values $\boldsymbol{v}$ as follows

$$v_i = \max\left[0.5, \exp\left(-\frac{\sum_{(t,n)\in\nu_i} \tilde{y}_{n,t}}{\sigma_v}\right)\right] \tag{13}$$

where σ_w, σ_v are fixed parameters (see [23]).

3.4. Estimation algorithm

The minimization of the convex function $\mathcal{C}(\boldsymbol{t})$ in (7) can be achieved using many convex programming algorithms [12, 24–26]. In this paper, we consider the ADMM variant proposed in [25] that has shown good performance in several fields [7, 27–30] while requiring a reduced computational cost. This algorithm is theoretically ensured to reach a minimum of $\mathcal{C}(\boldsymbol{t})$. More details regarding this algorithm and its convergence properties are available in [25, 26].

4. RESULTS

4.1. Results on synthetic data

This section assesses the proposed approach using a synthetic bowling data generated using a real physical scene from the Middlebury dataset [22, 31]. The depth and reflectivity images in Fig. 1 have been used to generate a $123 \times 139 \times 300$ data cube following model (1) while considering a real impulse response $g(.)$ and $b_n = 4, \forall n$. The proposed algorithm, denoted Nonlocal Restoration of 3D (NR3D) images, is evaluated while varying the signal number of photons-per-pixel (PPP) and the signal-to-background (SBR) ratio (ratio between signal and background counts) as presented in Table 1. NR3D is run using $(r_b, c_b, t_b, h) = (4, 4, 50, 5)$ and is compared to the classical cross-correlation approach applied to noisy data (denoted by classical) and background-free data (denoted by BF-classical or BFC). The NR3D

regularization parameters are manually selected to provide best visual results when testing the following intervals $\tau_1 = (1, 10, 100)$ and $\tau_2 = (0.01, 0.1, 1)$. Table 1 shows the $\text{SRE} = 10\log_{10}\left(\frac{||\boldsymbol{x}||^2}{||\boldsymbol{x}-\widehat{\boldsymbol{x}}||^2}\right)$ results, where $\boldsymbol{x}$ (resp. $\widehat{\boldsymbol{x}}$) is the reference (resp. estimated) depth or reflectivity image obtained using BFC on the highest Signal PPP data. This Table highlights the benefit of NR3D, which performs better than the BF-classical as it uses the information of adjacent pixels to restore the data. Note finally that negative reflectivity SREs are due to the presence of missing pixels for reduced PPP.

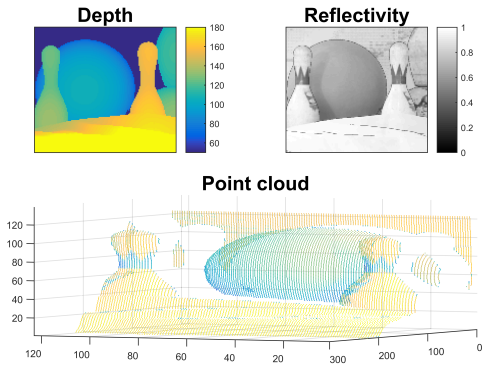

Fig. 1. Synthetic image (123×139 pixels) of a bowling scene. (Top-left) Depth map, (top-right) reflectivity and (bottom) point cloud combining depth and reflectivity.

Table 1. SRE (in dB) of the restored depth and reflectivity images w.r.t. SBR and signal photon-per-pixel (ppp).

Signal PPP		5	2	0.8	0.4	0.2
SBR		1.25	0.5	0.2	0.1	0.05
Depth	BFC	17.9	8.7	3.6	1.9	1.0
	Class.	11.5	5.3	2.9	2.2	1.9
	NR3D	**19.8**	**14.0**	**11.0**	**7.5**	**5.0**
Reflect.	BFC	7.3	3.5	-0.4	-3.5	-6.9
	Class.	6.6	1.4	-6.5	-13.1	-19.6
	NR3D	**13.3**	**13.0**	**8.4**	**9.8**	**3.2**

4.2. Results on real data

This section highlights the benefit of NR3D to restore sparse data obtained under reduced acquisition times. The considered data is a (142×142 pixels) real image of a life-sized polystyrene head acquired at a distance of 40m in 2014 on the Edinburgh Campus of Heriot-Watt University. The data was acquired using a large acquisition time of 30ms per-pixel (approximately 10 minutes for full image). However, the TCSPC system [14, 32] delivers time tagged data allowing the construction of histograms with reduced acquisition times (see [33] for more details regarding the imaging system). We then use NR3D to restore data obtained with 6ms, 300μs and 60μs, and compare the results to the classical algorithm, and RDI-TV [7]. Note that RDI-TV assumes the presence of one peak and known missing pixel positions, i.e., it is optimized for this scenario and can be seen as a reference (see [7] for more details). Fig. 2 shows the depth maps obtained using the three algorithms. As expected, the classical algorithm presents bad results when reducing the acquisition time. Although NR3D assumes the presence of multi-peaks, it still performs very well in presence of one peak and delivers results that are of similar quality to RDI-TV. This highlights the robustness of NR3D to missing pixels.

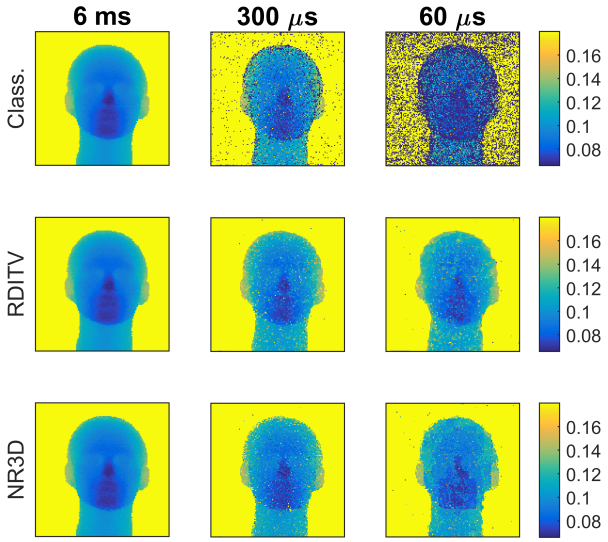

Fig. 2. Depth maps (142×142 pixels) of a life-sized polystyrene head acquired using different acquisition times. (First row) classical cross-correlation, (second row) RDI-TV, (third row) proposed NR3D algorithm.

5. CONCLUSIONS

This paper presented a new optimization based algorithm to restore single-photon 3D images. The method constructs a convex cost-function accounting for the Poisson statistics of the data, the non-local correlations between pixels and the local sparsity of detected depths. The resulting problem was solved using a fast ADMM algorithm that has good convergence properties. The approach was validated using synthetic and real data showing its benefit for processing sparse data corrupted with a high background level. It is worth noting that the approach assumes the presence of multi-peaks, an interesting property which was not highlighted here for space limitations. In addition, the approach can use the information of other modalities to set the weights, which allows its future use to perform multi-modal data fusion. Future work includes the application of this method to restore 3D images acquired through obscurants such as water, fog or smoke.

6. REFERENCES

[1] A. M. Pawlikowska, A. Halimi, R. A. Lamb, and G. S. Buller, "Single-photon three-dimensional imaging at up to 10 kilometers range," *Opt. Express*, vol. 25, no. 10, pp. 11 919–11 931, May 2017.

[2] D. Shin, F. Xu, F. N. C. Wong, J. H. Shapiro, and V. K. Goyal, "Computational multi-depth single-photon imaging," *Opt. Express*, vol. 24, no. 3, pp. 1873–1888, Feb 2016.

[3] R. Tobin, A. Halimi, A. McCarthy, X. Ren, K. J. McEwan, S. McLaughlin, and G. S. Buller, "Long-range depth profiling of camouflaged targets using single-photon detection," *Optical Engineering*, vol. 57, pp. 031 303 (1–10), 2017.

[4] A. Halimi, A. Maccarone, A. McCarthy, S. McLaughlin, and G. S. Buller, "Object depth profile and reflectivity restoration from sparse single-photon data acquired in underwater environments," *IEEE Trans. Comput. Imaging*, vol. 3, no. 3, pp. 472–484, 2017.

[5] S. Hernandez-Marin, A. M. Wallace, and G. J. Gibson, "Multilayered 3D lidar image construction using spatial models in a bayesian framework," *IEEE Trans. Pattern Anal. Mach. Intell.*, vol. 30, no. 6, pp. 1028–1040, June 2008.

[6] A. Halimi, R. Tobin, A. McCarthy, S. McLaughlin, and G. S. Buller, "Restoration of multilayered single-photon 3D lidar images," in *Proc. EUSIPCO*, 2017, pp. 708–712.

[7] A. Halimi, Y. Altmann, A. McCarthy, X. Ren, R. Tobin, G. S. Buller, and S. McLaughlin, "Restoration of intensity and depth images constructed using sparse single-photon data," in *Proc. EUSIPCO*, 2016, pp. 86–90.

[8] P. Sprechmann, I. Ramirez, G. Sapiro, and Y. C. Eldar, "C-Hilasso: A collaborative hierarchical sparse modeling framework," *IEEE Trans. Signal Process.*, vol. 59, no. 9, pp. 4183–4198, Sept 2011.

[9] H. K. Aggarwal and A. Majumdar, "Hyperspectral unmixing in the presence of mixed noise using joint-sparsity and total variation," *IEEE J. Sel. Topics Appl. Earth Observat. Remote Sens.*, vol. 9, no. 9, pp. 4257–4266, Sept 2016.

[10] M. D. Iordache, J. M. Bioucas-Dias, and A. Plaza, "Collaborative sparse regression for hyperspectral unmixing," *IEEE Trans. Geosci. Remote Sens.*, vol. 52, no. 1, pp. 341–354, Jan 2014.

[11] S. Boyd, N. Parikh, E. Chu, B. Peleato, and J. Eckstein, "Distributed optimization and statistical learning via the alternating direction method of multipliers," *Found. Trends Mach. Learn.*, vol. 3, no. 1, pp. 1–122, Jan 2011.

[12] M. Figueiredo and J. Bioucas-Dias, "Restoration of Poissonian images using alternating direction optimization," *IEEE Trans. Image Process.*, vol. 19, no. 12, pp. 3133–3145, Dec 2010.

[13] M.-D. Iordache, J. Bioucas-Dias, and A. Plaza, "Total variation spatial regularization for sparse hyperspectral unmixing," *IEEE Trans. Geosci. Remote Sens.*, vol. 50, no. 11, pp. 4484–4502, Nov. 2012.

[14] A. McCarthy, X. Ren, A. D. Frera, N. R. Gemmell, N. J. Krichel, C. Scarcella, A. Ruggeri, A. Tosi, and G. S. Buller, "Kilometer-range depth imaging at 1550 nm wavelength using an InGaAs/InP single-photon avalanche diode detector," *Opt. Express*, vol. 21, no. 19, pp. 22 098–22 113, Sep 2013.

[15] X. Ren, P. W. R. Connolly, A. Halimi, Y. Altmann, S. McLaughlin, I. Gyongy, R. K. Henderson, and G. S. Buller, "High-resolution depth profiling using a range-gated CMOS SPAD quanta image sensor," *Opt. Express*, vol. 26, no. 5, pp. 5541–5557, Mar 2018.

[16] S. Hernandez-Marin, A. Wallace, and G. Gibson, "Bayesian analysis of Lidar signals with multiple returns," *IEEE Trans. Pattern Anal. Mach. Intell.*, vol. 29, no. 12, pp. 2170–2180, Dec. 2007.

[17] Y. Altmann, X. Ren, A. McCarthy, G. S. Buller, and S. McLaughlin, "Lidar waveform based analysis of depth images constructed using sparse single photon data," *IEEE Trans. Image Process.*, vol. 25, no. 5, pp. 1935–1946, Mar. 2015.

[18] D. Shin, J. H. Shapiro, and V. K. Goyal, "Computational single-photon depth imaging without transverse regularization," in *Proc. IEEE Int. Conf. Image Process. (ICIP)*, Sept 2016, pp. 973–977.

[19] A. Buades, B. Coll, and J. M. Morel, "A review of image denoising algorithms, with a new one," *Multiscale Modeling & Simulation*, vol. 4, no. 2, pp. 490–530, 2005.

[20] K. Dabov, A. Foi, V. Katkovnik, and K. Egiazarian, "Image denoising by sparse 3-D transform-domain collaborative filtering," *IEEE Trans. Image Process.*, vol. 16, no. 8, pp. 2080–2095, Aug 2007.

[21] J. Salmon, Z. Harmany, C.-A. Deledalle, and R. Willett, "Poisson noise reduction with non-local PCA," *Journal of Mathematical Imaging and Vision*, vol. 48, no. 2, pp. 279–294, 2014.

[22] J. Rapp and V. K. Goyal, "A few photons among many: Unmixing signal and noise for photon-efficient active imaging," *IEEE Trans. Comput. Imaging*, vol. 3, no. 3, pp. 445–459, Sept. 2017.

[23] C. Lanaras, J. Bioucas-Dias, E. Baltsavias, and K. Schindler, "Super-resolution of multispectral multiresolution images from a single sensor," in *Large Scale Computer Vision for Remote Sensing Imagery-EARTHVISION'17*, Heidelberg, Honolulu, Hawaii, 2017.

[24] P. L. Combettes and J.-C. Pesquet, "A proximal decomposition method for solving convex variational inverse problems," *Inverse Problems*, vol. 24, no. 6, p. 065014, 2008.

[25] M. Afonso, J. Bioucas-Dias, and M. Figueiredo, "An augmented lagrangian approach to the constrained optimization formulation of imaging inverse problems," *IEEE Trans. Image Process.*, vol. 20, no. 3, pp. 681–695, March 2011.

[26] L. Boyd, Sand Vandenberghe, *Convex Optimization*. New York, NY, USA: Cambridge University Press, 2004.

[27] J. Bioucas-Dias and M. Figueiredo, "Alternating direction algorithms for constrained sparse regression: Application to hyperspectral unmixing," in *Proc. IEEE GRSS Workshop on Hyperspectral Image and SIgnal Processing: Evolution in Remote Sensing (WHISPERS)*, June 2010, pp. 1–4.

[28] A. Halimi, J. M. Bioucas-Dias, N. Dobigeon, G. S. Buller, and S. McLaughlin, "Fast hyperspectral unmixing in presence of nonlinearity or mismodeling effects," *IEEE Transactions on Computational Imaging*, vol. 3, no. 2, pp. 146–159, June 2017.

[29] J. Ying, H. Lu, Q. Wei, J. F. Cai, D. Guo, J. Wu, Z. Chen, and X. Qu, "Hankel matrix nuclear norm regularized tensor completion for n-dimensional exponential signals," *IEEE Transactions on Signal Processing*, vol. 65, no. 14, pp. 3702–3717, July 2017.

[30] W. J. Zeng and H. C. So, "Outlier-robust matrix completion via ell_p -minimization," *IEEE Transactions on Signal Processing*, vol. 66, no. 5, pp. 1125–1140, March 2018.

[31] D. Scharstein and C. Pal, "Learning conditional random fields for stereo," in *2007 IEEE Conference on Computer Vision and Pattern Recognition*, June 2007, pp. 1–8.

[32] A. M. Wallace, J. Ye, N. Krichel, A. McCarthy, R. Collins, and G. S. Buller, "Full waveform analysis for long-range 3d imaging laser radar," *EURASIP Journal on Advances in Signal Processing*, vol. 2010, no. 1, p. 896708, Dec. 2010.

[33] A. McCarthy, R. J. Collins, N. J. Krichel, V. Fernández, A. M. Wallace, and G. S. Buller, "Long-range time-of-flight scanning sensor based on high-speed time-correlated single-photon counting," *Appl. Opt.*, vol. 48, no. 32, pp. 6241–6251, Nov 2009.